AGU PUBLICATIONS

JGR

Journal of Geophysical Research: Atmospheres

RESEARCH ARTICLE

10.1002/2017JD026467

Key Points:

- We address the relationship between key cloud field macroscale properties: albedo and cloud fraction
- We present a new heuristic model for shallow cumulus size distribution and optical properties
- Large eddy and heuristic models both suggest oscillations in the power law cloud size distribution

Correspondence to:
G. Feingold,
graham.feingold@noaa.gov

Citation:
Feingold, G., J. Balsells, F. Glassmeier, T. Yamaguchi, J. Kazil, and A. McComiskey (2017), Analysis of albedo versus cloud fraction relationships in liquid water clouds using heuristic models and large eddy simulation, *J. Geophys. Res. Atmos.*, *122*, 7086–7102, doi:10.1002/2017JD026467.

Received 6 JAN 2017
Accepted 22 JUN 2017
Accepted article online 28 JUN 2017
Published online 12 JUL 2017

Analysis of albedo versus cloud fraction relationships in liquid water clouds using heuristic models and large eddy simulation

Graham Feingold[1], **Joseph Balsells**[2], **Franziska Glassmeier**[1,3], **Takanobu Yamaguchi**[1,2], **Jan Kazil**[1,2], **and Allison McComiskey**[1]

[1]Chemical Sciences Division, NOAA Earth System Research Laboratory, Boulder, Colorado, USA, [2]CIRES, University of Colorado Boulder, Boulder, Colorado, USA, [3]National Research Council, Washington, D. C., USA

Abstract The relationship between the albedo of a cloudy scene $\mathcal{A}$ and cloud fraction f_c is studied with the aid of heuristic models of stratocumulus and cumulus clouds. Existing work has shown that scene albedo increases monotonically with increasing cloud fraction but that the relationship varies from linear to superlinear. The reasons for these differences in functional dependence are traced to the relationship between cloud deepening and cloud widening. When clouds deepen with no significant increase in f_c (e.g., in solid stratocumulus), the relationship between $\mathcal{A}$ and f_c is linear. When clouds widen as they deepen, as in cumulus cloud fields, the relationship is superlinear. A simple heuristic model of a cumulus cloud field with a power law size distribution shows that the superlinear $\mathcal{A}$-f_c behavior is traced out either through random variation in cloud size distribution parameters or as the cloud field oscillates between a relative abundance of small clouds (steep slopes on a log-log plot) and a relative abundance of large clouds (flat slopes). Oscillations of this kind manifest in large eddy simulation of trade wind cumulus where the slope and intercept of the power law fit to the cloud size distribution are highly correlated. Further analysis of the large eddy model-generated cloud fields suggests that cumulus clouds grow larger and deeper as their underlying plumes aggregate; this is followed by breakup of large plumes and a tendency to smaller clouds. The cloud and thermal size distributions oscillate back and forth approximately in unison.

1. Introduction

Important cloud field properties relevant to climate studies include the albedo of a partially or fully cloudy scene $\mathcal{A}$ comprising (i) the effective cloud albedo $\mathcal{A}_c$, which accounts for clouds that directly reflect solar energy back to space, atmospheric opacity to downwelling shortwave radiation, and atmospheric opacity to shortwave radiation upwelling from the surface [*Schneider and Dickinson*, 1976; *Donohoe and Battisti*, 2011]; (ii) a combination of the underlying surface albedo and clear-sky atmospheric albedo, accounting for multiple reflections $\mathcal{A}_s$; and (iii) the cloud fraction f_c. The general relationship

$$\mathcal{A} = f_c\mathcal{A}_c + (1 - f_c)\mathcal{A}_s \tag{1}$$

has been noted in early papers [e.g., *Schneider and Dickinson*, 1976; *Charlock and Ramanathan*, 1985]. The endpoints of this relationship are defined by $\mathcal{A}_s$ for $f_c = 0$ and $\mathcal{A}_c$ for $f_c = 1$. Satellite remote sensing of a number of marine stratocumulus basins by the Moderate Resolution Imaging Spectroradiometer (MODIS) and Clouds and the Earth's Radiant Energy System spectrometers suggests a linear relationship between $\mathcal{A}$ and f_c [*Bender et al.*, 2011] for 1° × 1° monthly averages, while a more recent analysis of *all* clouds between 60°S and 60°N from the same instruments and averaging scales exhibits a characteristic curvature between the endpoints, which has been described by *Engström et al.* [2015] as "exponential." (We will refer to it as superlinear.)

A recent paper explored the $\mathcal{A}$-f_c relationship in cloud resolving and large eddy simulations of shallow boundary layer clouds—primarily stratocumulus clouds [*Feingold et al.*, 2016]. There, the authors showed $\mathcal{A}$ versus f_c relationships based on a large number of simulations (220) generated with different initial conditions—thermodynamic and aerosol/cloud condensation nucleus concentrations—as well as different covariability between thermodynamic and aerosol conditions. That paper served to illustrate two key points:

1. The relative robustness of the $\mathcal{A}$-f_c relationships suggests that it is a useful framework for exploring process understanding of clouds and cloud field properties and how they manifest in this framework.
2. The aerosol influence on the $\mathcal{A}$-f_c relationship manifested differently depending on the covariabilty of thermodynamic and aerosol conditions, suggesting that $\mathcal{A}$-f_c relationships might be a useful framework for studying the detectability of the aerosol signal via its influence on cloud field properties.

The question addressed in this paper is as follows: *What factors control the shape of the* $\mathcal{A}$-f_c *relationship?* The motivation lies in the fact that the $\mathcal{A}$-f_c relationship addresses parameters that are at the heart of the cloud radiative effect. The relative robustness of the relationship in a wide variety of cloud fields and regimes suggests that it can be exploited to facilitate quantification of the cloud radiative effect. To the extent that such relationships are indeed well defined, understanding the cloud field properties and processes that shape the relationship would be worthwhile. Other questions to consider are the dependence of these relationships on cloud regime and averaging scale, topics that will be deferred to a later study.

The $\mathcal{A}$-f_c relationship has been used as a means of diagnosing climate model performance [e.g., *Bender et al.*, 2011] and has been proposed as a framework for investigating the radiative effect of aerosol-cloud interactions. *Feingold et al.* [2016] argued for top-down or Newtonian approaches to understand aerosol-cloud interactions and their influence on planetary albedo; higher-order relationships such as $\mathcal{A}$-f_c are an expression of this top-down approach. The more familiar bottom up or Darwinian approach [e.g., *Ghan et al.*, 2016], while appealing, is complicated by the myriad derivatives in a long chain rule expansion that are often poorly constrained by measurement. We have argued that advances in our understanding will take place through a merging of both of these approaches [*Harte*, 2002; *Feingold et al.*, 2016].

The paper is organized as follows. First, we present two heuristic models of stratocumulus and cumulus cloud fields that serve to elucidate $\mathcal{A}$-f_c relationships. We show that the fundamental reason for superlinear responses of $\mathcal{A}$ to f_c is rooted in the documented power law relationship between cloud depth and cloud width, i.e., the fact that clouds become wider as they grow deeper [*Malkus and Simpson*, 1964]. In this regard, stratocumulus and cumulus systems offer opportunities for contrasting behavior. A simple heuristic model of a cumulus cloud field that conforms to a power law size distribution shows that the superlinear $\mathcal{A}$-f_c behavior emerges naturally either when cloud distribution power law slope and intercept vary randomly or when the cloud field evolves from a relative abundance of small clouds (steep, negative slope, and large intercept on a log-log plot) to a relative abundance of large clouds (shallow, negative slope, and small intercept). This is supported by large eddy simulation of trade wind cumulus, which shows that the slope and intercept of the power law fit to the cloud size distribution do in fact covary in this manner. Finally, through further analysis of large eddy simulation (LES) output, we provide possible explanations for the coevolution of power law slope and intercept and their oscillation.

2. Marine Boundary Layer Clouds

Stratocumulus clouds cover large areas of the oceans and are typically found on the western coasts of the major continents where cold waters and subsiding warm air combine to generate cloud fields with high f_c. Further west, the cloud field becomes progressively more broken as warmer waters and weaker subsidence allow the development of cumulus cloud fields with lower f_c. Pockets of open cells sometimes appear in high f_c stratocumulus regions as a result of precipitation [*Stevens*, 2005; *Sharon et al.*, 2006; *Xue et al.*, 2008; *Wang and Feingold*, 2009; *Wood*, 2012]. Cloud-resolving modeling of a marine boundary layer cloud system transitioning from a high f_c, nonprecipitating state to a lower f_c, precipitating state is shown in Figure 1. We note that there is a smooth transition in the $\mathcal{A}$-f_c relationship as one moves from high to low f_c and that the path traced out by these points is dependent on the definition of f_c. Points are color coded by the relative cloud radiative effect, rCRE, a quantity of high relevance to clouds and climate. Most likely by chance, the results for f_c based on a (visible) cloud optical depth $\tau_c > 5$ are remarkably similar to the best fit of the data by *Engström et al.* [2015] derived from space-based data for all clouds. Rather than focus on the similarities, we use these as illustrations of observed and modeled $\mathcal{A}$-f_c relationships and probe into factors (methodological, meteorological, macrophysical, microphysical, and radiative) that affect the relationship [see also *Feingold et al.*, 2016].

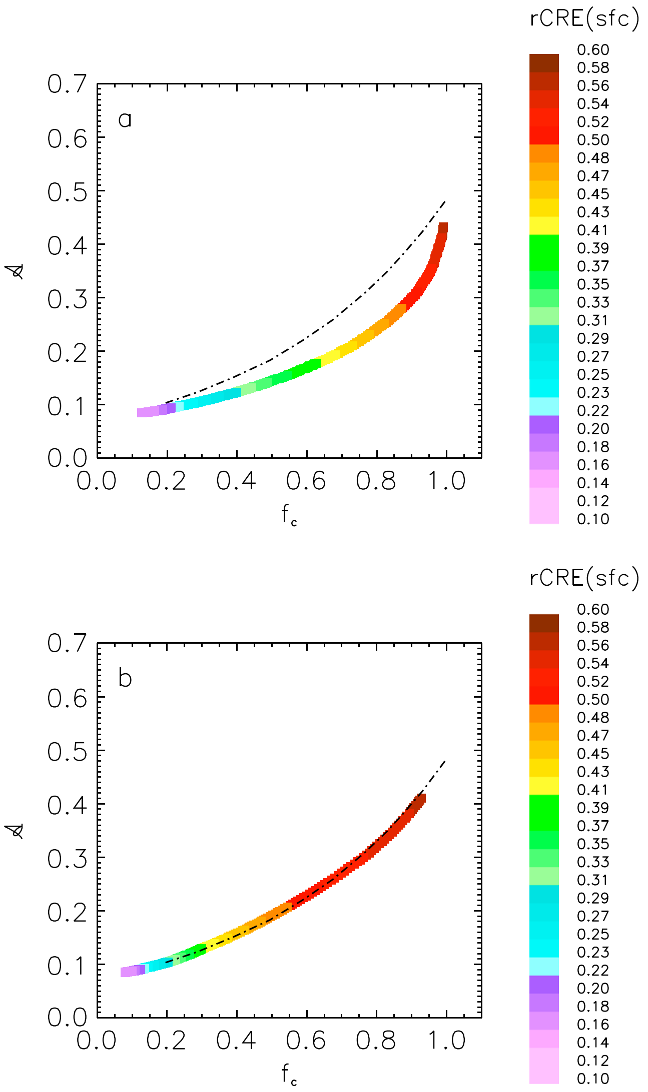

Figure 1. Illustration of $\mathcal{A}$ versus f_c for a closed to open cell stratocumulus transition for (a) f_c defined based on cloud optical depth >2 and (b) f_c defined based on cloud optical depth >5. Symbols are colored by relative cloud radiative effect (rCRE = 1 - transmittance). The *Engström et al.* [2015] relationship is superimposed as reference but not for strict comparison.

In the results to be presented below, the *Engström et al.* [2015] relationship is superimposed on many figures. We stress that it is added simply as a reference curve from an existing publication showing superlinearity. It also serves as a consistent reference from one figure to the next. By including it we do not imply that direct comparison between the satellite observations and our heuristic/large eddy modeling is being undertaken, nor that it is warranted, especially considering the differences in aggregation scale, analysis methods, and regimes considered. A rigorous comparison between observed and modeled $\mathcal{A}$-f_c relationships is deferred to a later study.

3. Simple Models

3.1. Relationship Between Cloud Deepening and Cloud Widening

We start with equation (1) and consider the fact that $\mathcal{A}_c$ is typically strongly related to liquid water path L, which is in turn a function of cloud depth. We ignore for now contributions of aerosol-related cloud brightening expressed generically by N, an unspecified number concentration related to aerosol or drop concentration.

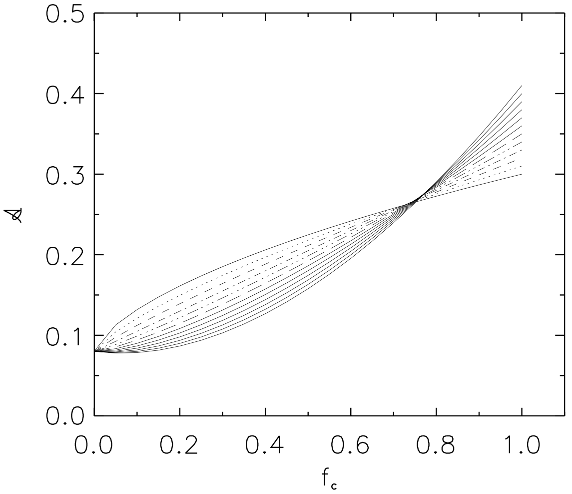

Figure 2. Theoretical curves for $\mathcal{A}$ versus f_c based on equations (1) and (2). The curvature changes from concave up for $\delta > 0$ to a linear relationship for $\delta = 0$ and then to concave down for $\delta < 0$. Here γ and δ change in unison such that smaller γ are associated with smaller δ. Approximate values of γ and δ were derived from analysis of large eddy simulation output from *Feingold et al.* [2015]. Typical values are $\gamma = 0.37$ and $\delta = 0.55$. Here the ranges of γ and δ are $0.30 < \gamma < 0.41$ and $-0.3 < \delta < 0.8$, respectively. Concave upward curvature increases with increasing δ.

(Influence of N and its covariability with meteorology was discussed in *Feingold et al.* [2016].) As noted earlier [e.g., *Bender et al.*, 2011], equation (1) can be rewritten as

$$\mathcal{A} = f_c(\mathcal{A}_c - \mathcal{A}_s) + \mathcal{A}_s \tag{2}$$

implying that if $\mathcal{A}_c$ is independent of f_c, then one can expect a linear relationship between $\mathcal{A}$ and f_c. We consider the more general possibility that

$$\mathcal{A}_c = \gamma f_c^{\delta} \tag{3}$$

where we make no assumptions about the sign of δ, so that $\mathcal{A}_c$ might either increase or decrease with increasing f_c. Combining equations (1) and (3) produces a set of characteristic curves for $\mathcal{A}$ versus f_c as shown in Figure 2. It quickly becomes clear that the upward concavity exhibited by Figure 1 is associated with $\delta > 0$. Theoretically, one might expect cloud elements to become wider as they become deeper, a concept that has roots in well-defined cloud aspect ratios, where stronger and deeper convective elements tend to have a larger areal extent [e.g., *Malkus and Simpson*, 1964]. The authors are not aware of observations that indicate downward concavity in the $\mathcal{A}$ versus f_c relationship although rapidly rising convective clouds that entrain strongly could result in $\delta < 0$ as the clouds become progressively narrower as they deepen. The linear relationship between $\mathcal{A}$ and f_c (i.e., $\delta = 0$) does appear in analyses of stratocumulus [*Bender et al.*, 2011] where vertical growth is limited by strong capping inversions.

3.2. The Considine Model

We consider a simple model of stratocumulus [*Considine et al.*, 1997] that exhibits some success in capturing various macroscale properties of stratocumulus cloud fields. For example, *Wood and Hartmann* [2006] show that the Considine model generates a relationship between the homogeneity parameter γ_L (defined as the square of the ratio between the mean L and the standard deviation of L) and f_c that is, in the mean, remarkably close to the relationship obtained from MODIS data (their Figure 7).

The model considers a cloud field that is characterized by Gaussian variance (σ^2_{cb}) in the lifting condensation level or cloud base height. Cloud top height is assumed to be constant, and L is adiabatic. Equations relating the probability distribution function of cloud depth $P(z)$ and cloud fraction can then be developed as follows:

$$P(z) = \frac{1}{\sqrt{2\pi}\sigma_{\mathrm{cb}}}\exp\left[-\frac{(z-\bar{z})^2}{2\sigma^2_{\mathrm{cb}}}\right], \tag{4}$$

$$P(z)\mathrm{d}z = P(L)\mathrm{d}L, \tag{5}$$

$$L = \frac{qz^2}{2}, \tag{6}$$

where q is a temperature-dependent constant and is $\approx 2.2 \times 10^{-3}$ g m^{-4}.

Using equations (4)–(6), one can calculate $P(L)$ as

$$P(L) = \frac{(2qL)^{-1/2}}{\sqrt{2\pi}\sigma_{\text{cb}}} \exp\left[-\frac{((2L/A)^{1/2} - \bar{z})^2}{2\sigma_{\text{cb}}^2}\right] \tag{7}$$

[*Considine et al.*, 1997]. Because $P(L)$ is normalized, cloud fraction is then defined as

$$f_c = \int_{L_{\min}}^{L_{\max}} P(L)\mathrm{d}L. \tag{8}$$

The lower L boundary is typically related to the minimum detectable L measured by a microwave radiometer. The key variable in this analysis is σ_{cb}. Airborne studies [e.g., *Wood and Taylor*, 2001] have produced relationships between σ_{cb} and boundary layer properties such as boundary layer depth z_i or variance in boundary layer temperature and humidity. To explore the influence of σ_{cb} on the $\mathcal{A}$-f_c relationship, we solve equations (4)–(8) and define σ_{cb} based on *Wood and Taylor* [2001]

$$\sigma_{\text{cb}} = 0.051z_i - 8.4, \tag{9}$$

where units are in meters. This empirical equation was derived from three stratocumulus airborne campaigns.

In order to calculate $\mathcal{A}$, we require equations for $\mathcal{A}_c$. We first calculate (visible) cloud optical depth τ_c

$$\tau_c \approx 2\pi \int_z \int_r r^2 n(r)\mathrm{d}r\mathrm{d}z, \tag{10}$$

where $n(r)$ is the number of drops between radius r and $r+\Delta r$. Equation (10) can be combined with equation (6) and the definition of drop effective radius

$$r_e = \frac{\int r^3 n(r)\mathrm{d}r}{\int r^2 n(r)\mathrm{d}r} \tag{11}$$

to yield

$$\tau_c = \frac{9}{5}\frac{L}{r_e} \tag{12}$$

[*Stephens*, 1978; *Wood and Hartmann*, 2006], with L in g m^{-2} and r_e in micrometers. For simplicity we fix r_e to a constant value.

Cloud albedo $\mathcal{A}_c$ is calculated using a two-stream approximation as

$$\mathcal{A}_c = \frac{\frac{(1-g)}{\cos\theta_o}\tau_c}{2 + \frac{(1-g)}{\cos\theta_o}\tau_c}, \tag{13}$$

with asymmetry factor $g = 0.85$ [*Bohren*, 1980] and solar zenith angle θ_o. Unless otherwise stated, an overhead Sun is assumed ($\theta_o = 0$). Note that this relationship is for visible albedo, in contrast to the broadband albedo measurements considered in *Engström et al.* [2015]. The $\mathcal{A}$-f_c relationship is then constructed from the Considine model using equations (1) and (4)–(13).

In Figure 3 we show $\mathcal{A}$ versus f_c for an assumed $r_e = 10$ μm. The results exhibit sensitivity to the choice of z_i but perhaps even more so to the choice of $L_{\min}$ in equation (8) (Figure 3). Thus, knowledge of the boundary layer depth and a match of instrument detection limits will be important in model—observation comparisons. A value of $L_{\min} = 45$ g m^{-2} matches the *Engström et al.* [2015] relationship quite well for $z_i = 800$ m. We reiterate, however, that the goal here is to explore sensitivities to various model parameters rather than to match an observed relationship; differences could derive from a multitude of sources. The sensitivity of curvature to the lower bound of integration is also illustrated in Figure 1, where minimum optical depths of $\tau_{c,\min} = 2$ or 5 were applied. For reference, $L_{\min} = 15$ g m^{-2} is approximately the same as $\tau_{c,\min} = 2.25$, and $L_{\min} = 35$ g m^{-2} is approximately the same as $\tau_{c,\min} = 5.25$ (assuming adiabatic liquid water, and drop effective radius $r_e = 12$ μm; see equation (12)).

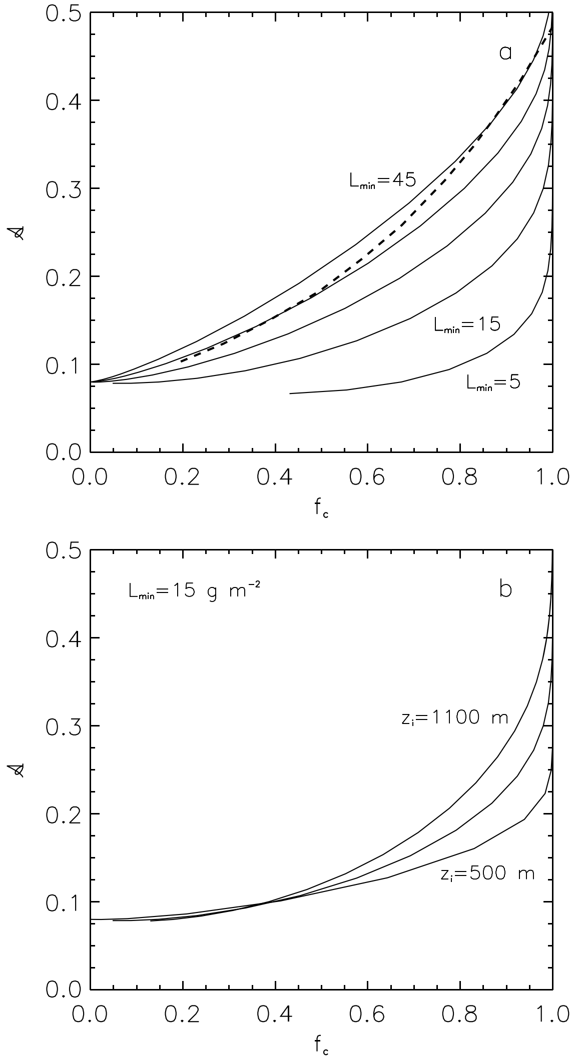

Figure 3. Theoretical curves for $\mathcal{A}$ versus f_c based on equations (1) and (4)–(13) (the Considine model): (a) inversion height $z_i = 800$ m and different values of L_{min} in equation (8). The lowest curve is for $L_{\text{min}} = 5$ g m^{-2}, increasing by increments of 10 g m^{-2} to 45 g m^{-2}. (b) Different values of z_i (500 m, 800 m, and 1100 m). The *Engström et al.* [2015] curve (dashed line) is superimposed for reference.

3.3. Cumulus Clouds

A broken cumulus cloud field has characteristics that lend themselves to a different approach. The cloud size distribution is known to be well described by a negative power law distribution in terms of cloud area a

$$P(a) = A\, a^{-b}, \tag{14}$$

where $P(a)$ is the number of clouds between cloud area a and $a + da$ in units of m^{-2}. A power law distribution of cumulus cloud sizes has been documented with satellite observations [e.g., *Benner and Curry*, 1998; *Zhao and Di Girolamo*, 2007; *Koren et al.*, 2008] and large eddy simulations [*Neggers et al.*, 2003; *Jiang et al.*, 2009; *Dawe and Austin*, 2012; *Heus and Seifert*, 2013]. It also applies quite well to all clouds globally [*Wood and Field*, 2011]. Following from the discussion in section 1, we assume that cloud depth is a function of cloud area:

$$z = \alpha a^{\beta}. \tag{15}$$

We use

$$P(z)\text{d}z = P(a)\text{d}a \tag{16}$$

together with equation (15) to derive

$$P(z) = \frac{A}{\alpha^{b'}\beta} z^{b'-1}, \tag{17}$$

where

$$b' = (1 - b)/\beta.$$

For the special (and rare) case of adiabatic shallow cumulus, equations (6) and (17) yield

$$P(L) = \frac{A}{\alpha^{b'}\beta} 2^{(b'/2)-1}\, q^{-b'/2}\, L^{(b'/2)-1}. \tag{18}$$

The cloud field mean liquid water path $\bar{L}$ can (generally) be calculated as

$$\bar{L} = \frac{\int LP(L)\mathrm{d}L}{\int P(L)\mathrm{d}L}. \tag{19}$$

For the special case of adiabatic clouds

$$\bar{L} = \frac{(b'/2)}{(b'/2+1)} \frac{\left[L_{\max}^{(b'/2+1)} - L_{\min}^{(b'/2+1)}\right]}{\left[L_{\max}^{b'/2} - L_{\min}^{b'/2}\right]}. \tag{20}$$

In defining τ_c for adiabatic clouds we can equivalently to equation (12) fix N and use equations (10), (6), and (12) together with the definition of cloud liquid water content $q_c = 4/3\pi\rho_l r^3 N$ (ρ_l is the density of liquid water) to derive

$$\bar{\tau}_c = c\, N^{1/3}\bar{L}^{5/6} \tag{21}$$

[e.g., *Boers and Mitchell*, 1994], where $c \approx 0.07$ for N in cm^{-3} and L in g m^{-2}.

For the more realistic case where entrainment mixing dilutes q_c below the adiabatic value we assume that

$$q_c = -pz^2 + qz \tag{22}$$

or

$$L = -\frac{p\,z^3}{3} + \frac{qz^2}{2}, \tag{23}$$

[*Lu et al.*, 2009; *Feingold et al.*, 2013] where p is a positive valued, tunable parameter that sets the degree of subadiabaticity (cf. equation (6)) and is bounded such that $q_c \geq 0$. Since $z = f(L)$ is the solution to a cubic equation (only one of the roots of which is real) and dz/dL is not easily differentiated, equation (23) yields a significantly more complicated form of $P(L)$; we therefore integrate equation (19) numerically for $\bar{L}$. Cloud optical depth also takes on a more cumbersome form but can be calculated analytically as

$$\begin{aligned} \tau_c &= CN^{1/3} \int (-pz^2 + qz)^{2/3}\mathrm{d}z \\ &= CN^{1/3} \left[\frac{0.6z(qz(1-pz/q))^{2/3}\,{}_2F_1(-2/3,\ 5/3;\ 8/3;\ pz/q)}{(1-pz/q)^{2/3}}\right], \end{aligned} \tag{24}$$

with $\mathrm{C} = 2\pi\,(3/(4\pi\rho_l))^{2/3}$ and ${}_2F_1$ the hypergeometric function. Substituting $\bar{z} = f(\bar{L})$, equation (24) can be solved for $\bar{\tau}_c$ provided $pz/q < 1$, a condition easily met for shallow cumulus.

For both adiabatic and subadiabatic clouds, cloud albedo $\mathcal{A}_c$ is calculated using equation (13). Finally, we calculate f_c for both adiabatic and subadiabatic clouds as

$$f_c = \frac{\int_{a_{\min}}^{a_{\max}} aP(a)\mathrm{d}a}{L_x^2} = \frac{A}{(2-b)} \frac{\left[a_{\max}^{(2-b)} - a_{\min}^{(2-b)}\right]}{L_x^2}, \tag{25}$$

where $b \neq 2$ and L_x is the horizontal dimension of the square domain of interest.

To recapitulate, for adiabatic clouds we use equations (1), (25), and (13) with (21) to calculate $\mathcal{A}$ and f_c. In the case of subadiabatic clouds, we first solve equation (23) for $\bar{z}$ as a function of $\bar{L}$, considering only the real root. (In practice, we used an iterative root finder.) This solution is substituted into equation (24) to yield an expression for subadiabatic $\bar{\tau}_c$ as a function of N and $\bar{L}$ that replaces equation (21). Cloud albedo is calculated based on equation (13) and $\mathcal{A}$ is calculated from equation (1). In all cases we assume that $\mathcal{A}_s = 0.08$, appropriate for an ocean environment.

We note that the mean cloud albedo is calculated directly from the mean cloud optical depth, which could differ from the mean cloud albedo calculated directly from the albedos of the individual clouds. Given the

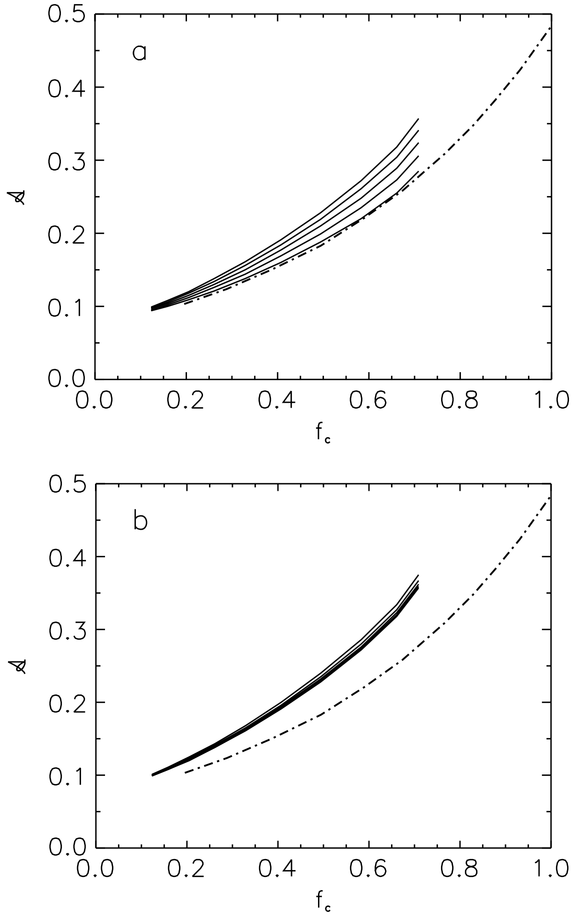

Figure 4. (a) Illustrative example of model curves for $\mathcal{A}$ versus f_c based on equations (13)–(25) (the Cumulus model) for different values of subadiabaticity p. (The topmost curve is the adiabatic case.) To achieve the range of $\mathcal{A}$ and f_c displayed, parameters A and b in equation (14) change in unison, i.e., large (small) values of A are associated with large (small) values of b indicating a shift from large numbers of small clouds (high f_c and $\mathcal{A}$) through small numbers of large clouds (low f_c and $\mathcal{A}$). The relationship between A and b is exponential: $A = 1.49 \times 10^{-5} e^{(12.3b)}$. The *Engström et al.* [2015] curve (dashed line) is superimposed for reference. (b) As in Figure 4a but for adiabatic clouds and considering the influence of solar zenith angle in the calculation of $\mathcal{A}_c$. Lines are for θ_o = 0, 30, 45, 60, and 80°. The highest curve is for $\theta_o = 80°$, and the lowest curve is for $\theta_o = 0°$.

approximately linear relationship between $\mathcal{A}_c$ and τ_c at small τ_c shown in (13), and the predominance of small clouds in the negative power law size distribution, particularly for the large values of b associated with cumulus clouds, the relationship between $\mathcal{A}_c$ and τ_c is expected to be linear. If deep clouds were to contribute significantly to τ_c (e.g., for small b), the heuristic model would create a high bias in $\mathcal{A}_c$ (and therefore $\mathcal{A}$) because by (13), $\mathcal{A}_c$ increases sublinearly with τ_c at large τ_c. For sufficiently large clouds the heuristic model will fail because pz/q will exceed unity. These caveats should be borne in mind when applying the current model. Nevertheless, the sensitivities of the $\mathcal{A}_c$-f_c relationship to the various model parameters are still expected to be valid.

Solution to the cumulus equation set provides a single ($\mathcal{A}$, f_c) point for given values of A and b. In order to achieve a range of $\mathcal{A}$ and f_c values, we vary A and b in a variety of ways. First, we consider a fairly intuitive covariation between A and b that represents populations of clouds dominated by larger or smaller clouds. $\mathcal{A}$-f_c relationships for adiabatic and subadiabatic conditions calculated in this manner are illustrated in Figure 4, with more details on parameter settings given in Figures 5 and 6 and their respective captions. In each case the covariability between A and b is quantified. The subadiabatic parameter p is applied to the cloud field and tuned such that the deepest clouds (with depth $z_{\max}$) have zero q_c at $z_{\max}$. The influence of p in Figure 4a

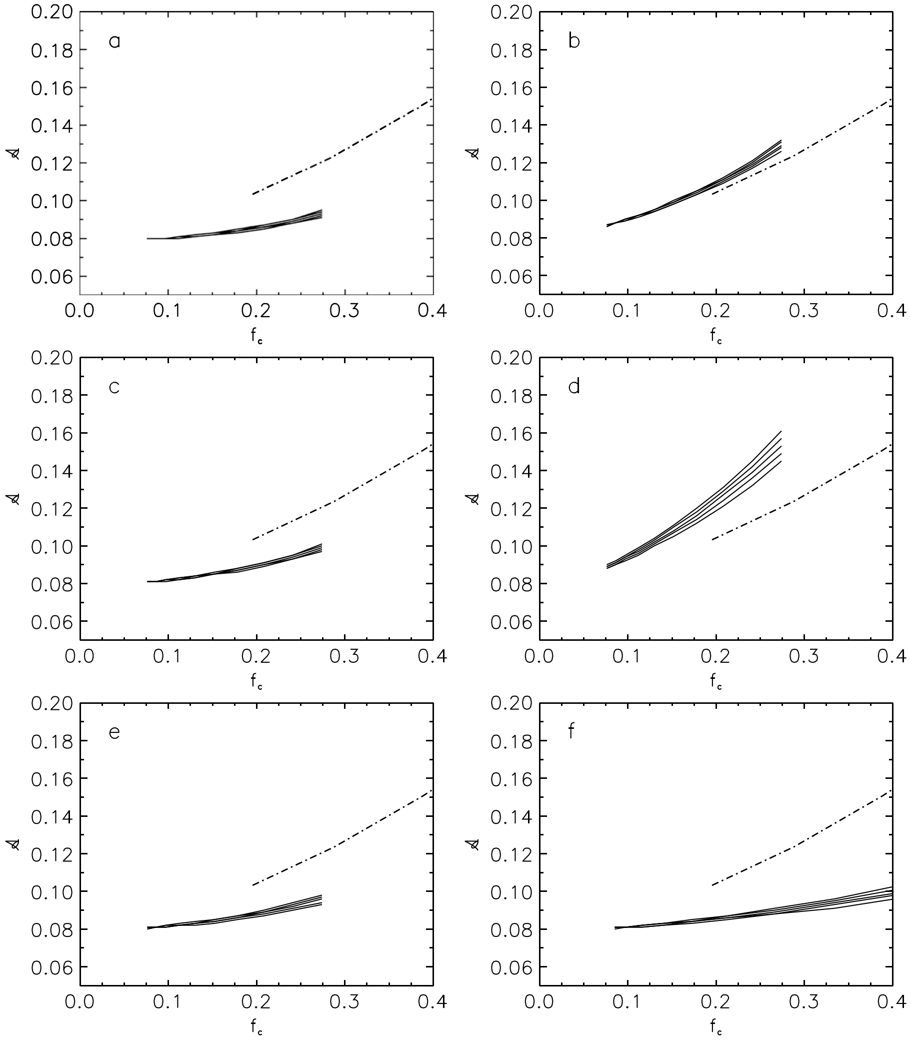

Figure 5. As in Figure 4a but for various parameter settings. Here $A = 5 \times 10^{-2} e^{(7.6b)}$. In all cases, $1.7 < b < 2.05$, minimum cloud area $a_{\min} = 300$ m^2, $\alpha = 10$, $z_{\min} = 50$ m. (a) $r_e = 12$ μm, $z_{\max} = 1500$ m, $\beta = 0.3$. (b) As in Figure 5a but $r_e = 5$ μm. (c) As in Figure 5a but $r_e = 10$ μm. (d) As in Figure 5c with $\beta = 0.5$. (e) As in Figure 5c but with $z_{\max} = 920$ m. (f) As in Figure 5c but with $a_{\max} = 3 \times 10^9$ m^2. (In Figure 5f, f_c reaches 0.51 but the f_c range is maintained to facilitate comparison with other panels and to demonstrate the sensitivity to $a_{\max}$.) Note the strong sensitivities to r_e, β, and $a_{\max}$, and that subadiabaticity is much more important at higher β when cloud depth increases more strongly with cloud area.

explains a significant amount of variability in the curvature of $\mathcal{A}$ versus f_c. Figure 4b explores the effect of solar zenith angle θ_o on the relationship for the adiabatic case and shows minimal influence for θ_o varying between 0° and 80°.

Collectively, Figures 4–6 demonstrate the main sensitivities of the model. First, comparing Figure 5 ($1.70 < b < 2.05$; smaller f_c) and Figure 6 ($1.35 < b < 1.70$; a large range of f_c), we note the strong sensitivity of f_c to b, with smaller b resulting in higher f_c. Second, the parameter β, which reflects the extent to which clouds deepen as they widen ($z = \alpha a^{\beta}$) has strong influence over the slope and curvature of the $\mathcal{A}$-f_c curves (cf. Figure 5a versus 5d). Similarly, microphysics, via r_e, also has significant influence (cf. Figure 5a versus 5b or Figure 6a versus 6d). The effect of subadiabaticity increases with increasing f_c (cf. Figures 5 and 6)

As is typical of power law models, we note strong sensitivity to assumed boundary conditions, e.g., maximum cloud area $a_{\max}$ (cf. Figures 6a and 6c). This should be borne in mind when comparing observations and model output, each with its own characteristic resolution and domain size.

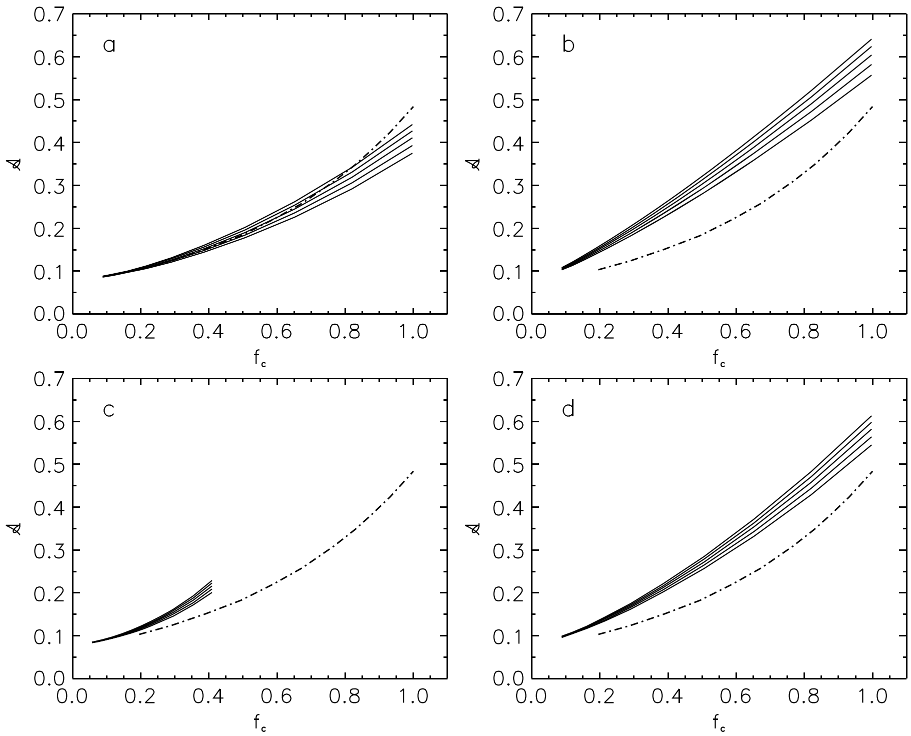

Figure 6. As in Figure 5 but for smaller b ($1.35 < b < 1.70$). Here $A = 7.5 \times 10^{-3} e^{(10b)}$. Note the larger f_c values compared to Figure 5. (a) $r_e = 10$ µm, $z_{\max} = 1500$ m, $\beta = 0.3$, $a_{\max} = 1.28 \times 10^9$. (b) As in Figure 6a but with $\beta = 0.5$. (c) As in Figure 6a but with $a_{\max} = 3 \times 10^8$ m^2. (d) As in Figure 6a but with $r_e = 5$ µm. As in Figure 5, strong sensitivities to β, r_e, and $a_{\max}$ are apparent.

Next we take a set of A and b parameters and sample random pairs such that there is *no preferred covariability* in A and b. Figure 7 shows that here too, superlinear curvature in the $\mathcal{A}$ versus f_c emerges, albeit weakly. This result is consistent with that of *Engström et al.* [2015] since their sampling of many different snapshots of cloud fields from different regimes and different stages of evolution is akin to a random sampling when all results are aggregated.

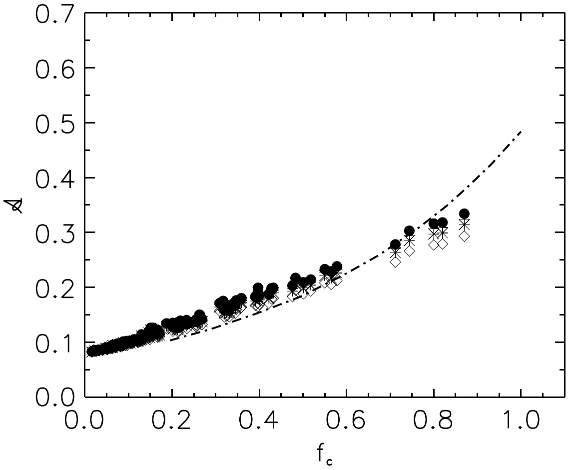

Figure 7. Cumulus model for random pairings of A and b drawn from a range of A and b that produces f_c in the range of interest. Other model parameter settings include $\beta = 0.3$, $a_{\min} = 300$ m^2, $a_{\max} = 3 \times 10^8$ m^2, and $r_e = 7$ µm. Symbols are used to represent subadiabaticity (filled circle is the adiabatic case). Note that this random pairing also produces super linear $\mathcal{A}$-f_c relationships. The *Engström et al.* [2015] curve (dashed line) is superimposed for reference.

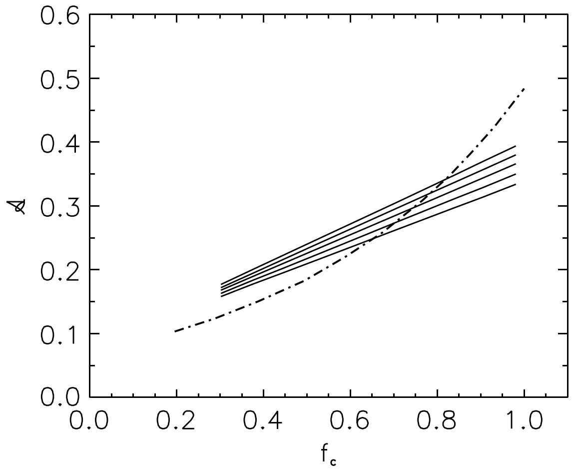

Figure 8. Cumulus model for constant slope ($b = 1.7$) but varying intercept A. Other model parameter settings include $\beta = 0.5$, $a_{\text{min}} = 300\ \text{m}^2$, $a_{\text{max}} = 3 \times 10^8\ \text{m}^2$, and $r_e = 10\ \mu\text{m}$. The slope of the lines is directly proportional to β. The *Engström et al.* [2015] curve (dashed line) is superimposed for reference.

In contrast to the use of covarying or random pairings of A and b, we can also achieve a range of $\mathcal{A}$ and f_c by simply varying A and holding b constant. In this case $\mathcal{A}$ is linearly dependent on f_c (Figure 8). The slope of the lines is directly proportional to β (as in Figure 5) and to a much weaker extent, to p.

4. Insights From Large Eddy Simulation

4.1. Covariability in Slope and Intercept of Cloud and Thermal Size Distributions

The simple cumulus cloud model suggests that if A and b (equation (14)) vary randomly, or covary such that $A \propto b$, then superlinear $\mathcal{A}$ versus f_c relationships emerge naturally, whereas when b is constant and A controls changes in $\mathcal{A}$ and f_c, a linear relationship emerges. But is there evidence for a relationship between A and b? To investigate this, we analyze large eddy simulation (LES) output from the Barbados Oceanographic and Meteorology Experiment (BOMEX), a well-studied trade wind cumulus case [e.g., *Siebesma et al.*, 2003]. The model used is the System for Atmospheric Modeling (SAM) [*Khairoutdinov and Randall*, 2003] with an isotropic grid spacing of 40 m, a time step of 2 s, and a domain size of 24 km × 24 km × 4 km. The model includes a two moment treatment of cloud water and rain water, as well as aerosol activation based on prognosed supersaturation. Details are described elsewhere [e.g., *Yamaguchi and Feingold*, 2015].

Applying a cloudy column definition when the visible optical depth exceeds 2, which excludes small optically thin fragments, cloud size distributions were calculated as two-dimensional projections. The trade wind cumulus clouds generated by the model follow an expected power law size distribution as in earlier studies [*Neggers et al.*, 2003; *Xue and Feingold*, 2006], as well as a power law dependence of cloud depth on cloud area (equation (15)) with $\beta \approx 0.3$. A value of $\beta = 0.3-0.4$ was also found by *Jiang et al.* [2009] when modeling trade wind cumulus clouds associated with the Rain in Cumulus over Oceans (RICO) field experiment [*Rauber et al.*, 2007]. Of particular interest is the time series of A and b (Figure 9a) which shows strong correlation between A and b ($r = 0.94$), supporting our assumption of covariability used ad hoc in section 3.3. The tight relationship between A and b is well approximated by an exponential function of the form $A = 3.4 \times 10^{-3} e^{11.8b}$ (Figure 9b). As cloud size distributions evolve in time, they can be seen to oscillate between relatively large numbers of small clouds (large A and b) to relatively large contributions of large clouds (small A and b, Figure 10). While the size distributions do not pivot around a well-defined point, they do tend to result in the lowest variability in the number of clouds of area $\approx 10^5\ \text{m}^2$. The linear relationship between $ln(A)$ and b (Figure 9b) is consistent with pivoting of the power law distribution displayed in the linear (in log-log space) cloud size distributions (Figure 10). In fact, it is trivial to show analytically that if a straight line pivots about a fixed point, then the change in the intercept parameter caused by the pivoting is a linear function of the change in the slope.

Power law fits were also applied to thermals, defined as regions of higher than average subcloud vapor mixing ratio q_v at the approximate midlevel of the boundary layer (280 m). (Thresholds on q_v are discussed below.) There is no perfect thermodynamic variable to identify thermals. Potential temperature θ can also be used but is problematic because higher up in the mixed layer the warmer θ air associated with buoyant thermals

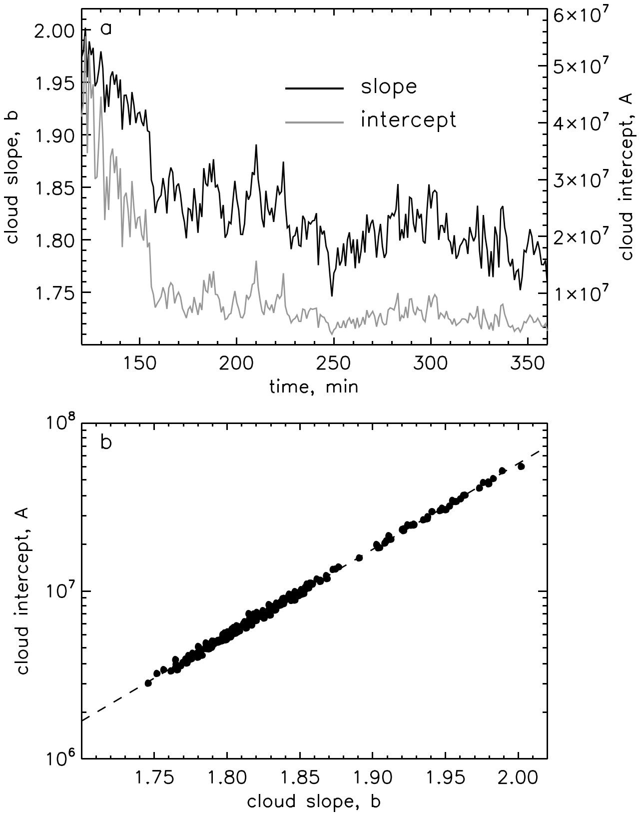

Figure 9. Large eddy simulation results for (a) time series of cloud power law size distribution parameters A (intercept) and b (slope). The correlation coefficient is 0.94. (b) A versus b showing that the A-b relationship is well described by an exponential function $A = 3.4 \times 10^{-3}\ e^{11.8b}$. (cf. similar relationships for Figures 4, 5, and 6.)

becomes conflated with warmer downward moving warm air from the free troposphere. Water vapor mixing ratio is preferable because moist boundary layer thermals are distinct from dry air mixing down from the free troposphere [*Lenschow and Stephens*, 1980]. The passive scalar method [*Dawe and Austin*, 2012] may be preferable. Various percentiles of q_v were tested, and results for the 95th percentile were selected for the analysis. It is noted that other definitions of thermals were also considered (including subcloud positive buoyancy); the results presented here for the midlevel subcloud q_v thermal sizing are representative. Results for other definitions of thermals are used to strengthen and clarify the arguments put forth (see below).

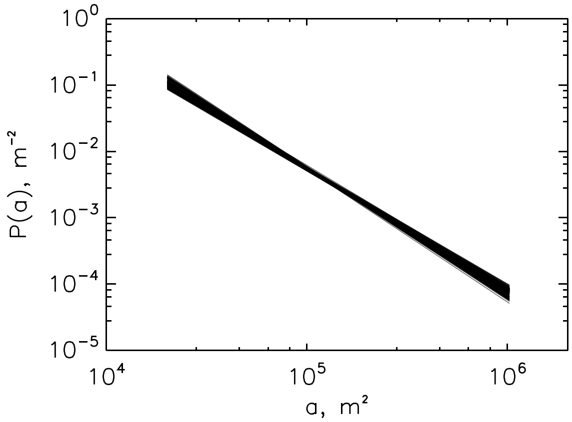

Figure 10. Power law size distribution fits from the model output in Figure 9. The size distributions evolve between states of relatively large numbers of small clouds to relatively large numbers of large clouds.

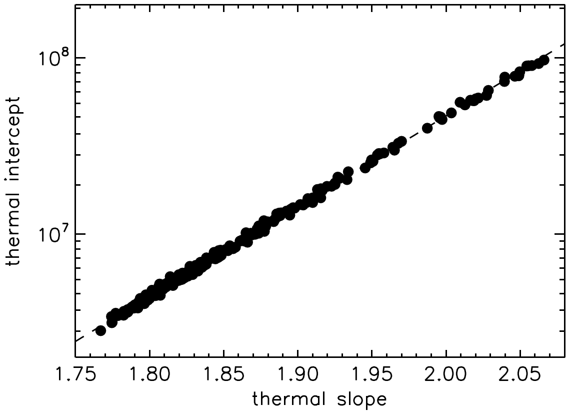

Figure 11. Thermal intercept parameter as a function of thermal slope parameter. The correlation coefficient is 0.92. As in Figure 9b an exponential function approximates well the relationship between intercept and slope: $A_t = 2.7 \times 10^{-3}\ e^{11.8 b_t}$ where A_t and b_t are the thermal intercept and slope parameters, respectively. Note that the exponential coefficient (i.e., the slope on the log linear plot) is the same (within round-off error) as that in Figure 9b.

Here too, the thermal size distributions follow a power law with the slope and intercept parameters covarying in unison (Figure 11). Remarkably, the slope/intercept parameters of the cloud and thermal size distributions are correlated (Figure 12). The correlation between cloud and thermal slope parameters over the 4 h period in Figure 9a is 0.86, at zero time lag (Figure 13). We experimented with different definitions of thermals and found that if thermals are defined by subcloud positive buoyancy (at the 75th percentile), then the positive time-lagged correlations fall off much more slowly than do the negative time- lagged correlations, perhaps indicating that despite a fairly high temporal correlation, *buoyant* thermal size distribution changes sometimes precede cloud size distribution changes (Figure 13).

A Fourier spectral analysis of the size distribution parameters exhibits two consistent peaks for both the cloud and thermal size distribution parameters: one at a periodicity of ≈80 min (associated with a similar peak in the Fourier spectrum of the inversion height) and one at ≈15 min (approximately the eddy turnover time). (Figures not shown.) The power spectra both exhibit significant variability, which might reflect the fact that some clouds are supported by multiple thermals. This might be at least partially related to the documented pulsations in individual trade wind cumulus clouds [*Heus et al.*, 2009; *Witte et al.*, 2014].

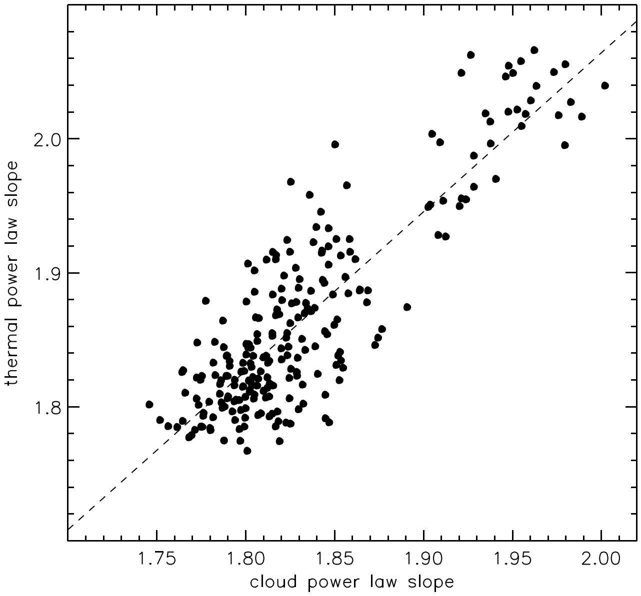

Figure 12. Thermal power law slope parameter as a function of cloud power law slope parameter. The best fit line is given by $y = -0.31 + 1.19x$. The correlation is 0.86.

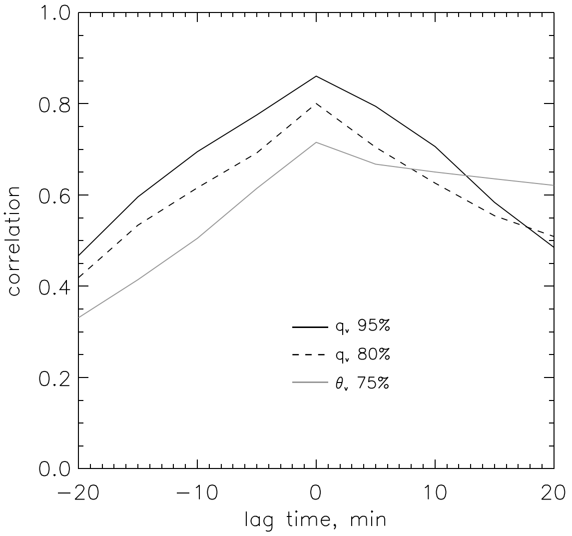

Figure 13. Lagged cross correlations between cloud and thermal slope parameters. The black solid line is associated with thermals defined by the 95th percentile of subcloud vapor, q_v. The dashed line is for thermals defined by the 80th percentile of subcloud q_v. The grey line is based on thermals defined by the 75th percentile of subcloud positive buoyancy θ_v' (where θ_v is the virtual potential temperature). The asymmetry in the latter suggests that buoyant thermal size distribution changes sometimes precede cloud size distribution changes.

4.2. Nature Versus Nurture

The coevolution of thermal and cloud size distributions raises the question of whether cloud development is driven by subcloud properties (“nature”) or the environmental conditions they encounter (“nurture”) [*Romps and Kuang*, 2010; *Dawe and Austin*, 2012]. *Romps and Kuang* [2010] analyzed tracers in a large eddy simulation of shallow convection (the same BOMEX case simulated here) and concluded that stochastic entrainment, rather than subcloud properties, determines the growth of convective elements. Using cloud-tracking analyses of the BOMEX case, and with the same model (but different microphysics) used here, *Dawe and Austin* [2012] concluded that cloud base properties determine the area and height achieved by clouds while entrainment controls their thermodynamic properties. The correlation between subcloud thermal and cloud size distributions elucidated in the current work is suggestive of nature being the primary driver of the cloud size distribution, in agreement with *Dawe and Austin* [2012].

To explore the possible role of nurture, we examined the size distributions of entities associated with positive q_v anomalies in *cloud-free regions above-cloud base*. Such entities are indicative of the mutual influence between clouds and their environment. These volumes were reduced to two-dimensional areas by averaging in the vertical and then sized. Here too, power law size distributions were determined to be appropriate. We found positive correlations between the size parameters of these above-cloud base q_v anomaly entities and the cloud size distribution parameters: for percentile thresholds of 75th and 90th the correlations between the slope parameters of the two size distributions are 0.30 and 0.82, respectively, over the 4 h period in Figure 9a. This result suggests that environmental conditions above-cloud base associated with detrainment/entrainment processes also influence cloud size, via their effect on cloud thermodynamics. Thus, in agreement with *Dawe and Austin* [2012], both nature and nurture influence the evolution of the cloud field.

4.3. Causality

The covariability of *A* and *b* representing the cycling from a cloud population with a relatively large number of small clouds to one with a relatively large number of large clouds is suggestive of a process by which small cloud (or thermal) elements aggregate to form larger clouds/thermals [*Malkus*, 1953; *Lopez*, 1977; *Lenschow and Stephens*, 1980], followed by a breakup into smaller clouds/thermals. A number of possible mechanisms via which this might occur have been explored. For example, we consider whether the formation of larger clouds (smaller *b*) results in a noticeable reduction in convective available potential energy (CAPE), which in turn might create conditions conducive to smaller clouds [*Nober and Graf*, 2005]. Rather than lagged correlations that might indicate a causal relationship, we find a high negative correlation (−0.85) between CAPE and slope b (smaller slopes or larger clouds are associated with higher CAPE, as expected) but at zero lag. The high correlation suggests a self-consistency of the system, which builds confidence, but the fact that the maximum occurs at zero lag makes it hard to infer causality.

We also find a negative correlation between subcloud instability and the slope of the thermal size distribution (−0.9; higher instability generates larger clouds) and between surface wind shear and b (−0.88; higher wind shear generates larger clouds)—both maximal at zero lag. Together, these correlations suggest that the cloud slope parameter b and its evolution are controlled by both thermodynamics (thermal evolution and vertical stratification) and dynamics (low-level convergence) through a complex interplay of processes acting at different spatiotemporal scales. Remarkably, these processes work together in such a way that b is robustly $\propto A$.

5. Summary

In recent years a top-down ("Newtonian") view of relationships between high-level cloud field properties has been proposed as a framework for understanding primary controls on cloud albedo $\mathcal{A}$, cloud fraction f_c, and the cloud radiative effect [*Bender et al.*, 2011; *Engström et al.*, 2015; *Feingold et al.*, 2016]. This study has focused on understanding some of the key controls of the shape of the $\mathcal{A}$-f_c relationship. To this end, two simple heuristic models have been applied: the first for stratocumulus [*Considine et al.*, 1997] and the second for shallow cumulus (presented herein). In addition, large eddy simulation of shallow cumulus cloud fields has been used to test some of the ideas emerging from the heuristic cumulus model.

The essence of the newly presented cumulus model (section 3.3) can be summarized as follows. The cloud size distribution is described by a power law, as is the relationship between cloud depth z and cloud area a. There is ample evidence in the literature for both assumptions. The model then uses a quadratic form of cloud water variation with height to connect liquid water path L to cloud depth and/or area. The parameter p (equation (23)) is modified to generate clouds of different subadiabaticty, with the requirement that cloud water mixing ratio is positive. We calculate a mean L for the cloud size distribution ($\bar{L}$) and, assuming a fixed r_e (or N), calculate a mean cloud optical depth ($\bar{\tau}_c$). A simple two-stream approximation is then applied to relate cloud albedo $\mathcal{A}_c$ and $\bar{\tau}_c$. For adiabatic conditions, integration is performed analytically. For subadiabatic conditions in which cloud water varies as $-pz^2 + qz$, $\bar{L}$ is integrated numerically; however, a new analytical relationship for $\tau_c = f(L, r_e)$ is derived (equation (24)). Cloud fraction f_c is integrated analytically.

The key results of this paper can be summarized as follows:

The primary control over the degree of curvature in the $\mathcal{A}$-f_c relationship is the extent to which clouds deepen as they widen. The stratocumulus model is used to show that a value of $\beta = 0$ in the $z = \alpha a^{\beta}$ relationship results in a linear $\mathcal{A}$-f_c relationship and that concave upward curvature in $\mathcal{A}$-f_c occurs when $\beta > 0$. This is verified for the cumulus model. The results help explain the *Bender et al.* [2011] linear relationship for stratocumulus, a regime in which cloud deepening is limited by a strong capping inversion, in accord with a low (but positive) β.

The cumulus model can reproduce superlinear behavior in the $\mathcal{A}$-f_c relationship when the intercept parameter A covaries with slope parameter b in the power law size distribution of clouds ($P(a) = Aa^{-b}$; Figure 4) or when A and b vary randomly. For the covarying A and b, the key cumulus model parameter settings are varied to explore the primary controls over the shape, curvature, and range of the $\mathcal{A}$-f_c relationship (Figures 5 and 6). Again, the β parameter is shown to be of central importance. Microphysical influences, expressed here by drop effective radius r_e, are also shown to be important; the rate of rise of the curves is inversely proportional to r_e. Thus, with clear characterization of measurements and methodology, the radiative effect of aerosol-cloud interactions should be detectable in this framework, particularly with supporting r_e and aerosol measurements.

As expected from power law relationships, results are strongly sensitive to limits of integration. It follows that any comparison between model (heuristic or other) and observations be keenly aware of resolution, domain size, and detection limits (of L or τ). In addition, the effects of three-dimensional radiation, while inherent to observations, will also need to be explored more rigorously than in the modeling study of *Feingold et al.* [2016]. These topics will be explored in future work. In this spirit, the observed relationship from *Engström et al.* [2015] has been used simply as a reference, since no attempt has been made to match instrument detection limits, aggregation scale, or resolution (Figure 1). Moreover, the Engström et al. study includes clouds from many different regimes, whereas the heuristic models are developed for shallow liquid clouds only. To the extent that shallow cumulus are expressed in the Engström et al. study, the simplest explanation for their superlinear $\mathcal{A}$-f_c behavior might be a random pairing of A and b rather than covariability in A and b, particularly because we expect data aggregation into 1° × 1°, monthly averages to obscure process level covariability in A and b.

Covariability between A and b used in the cumulus model is explored in large eddy simulation of a trade wind cumulus case study. We find that in the LES, A and b indeed vary in unison (correlation coefficient of 0.94) and that there is a well-defined exponential relationship between A and b (Figure 9b). The cloud size distributions are shown to oscillate between states of relatively high numbers of small clouds (large b, large A) and relatively large numbers of large clouds (small b, small A; Figure 10). An analysis of the size distribution of subcloud thermals is also shown to follow a power law size distribution with power and intercept parameters covarying much like in Figure 9b (Figure 11). The correlation between thermal and cloud size distribution parameters is 0.86, at zero lag (Figure 12), with only weak sensitivity to the definition of a thermal (Figure 13). The causal nature of the oscillating cloud size behavior thus appears to be rooted in the convective process itself, in accord with the idea that cloud thermals grow by aggregation [*Malkus*, 1953; *Lopez*, 1977; *Lenschow and Stephens*, 1980] but begin to break up when thermals are sufficiently large. We hypothesize that since larger thermals are more likely to produce larger clouds, the thermal aggregation/breakup process is likely to manifest in sequences of cloud size distributions experiencing Ostwald ripening and inverse Ostwald ripening processes (digestive ripening) [*Lee et al.*, 2007]. Thus, while it is generally assumed that cloud size distributions follow power laws with well-defined slope, the small variability in these slopes appears to be indicative of deeper underlying convective processes. This topic will be pursued in subsequent studies.

Acknowledgments
G. Feingold thanks Wayne Angevine for useful discussions. This research was supported by the Office of Biological and Environmental Research of the U.S. Department of Energy Atmospheric System Research Program Interagency Agreement DE-SC0016275. F. Glassmeier is the recipient of a National Research Council Research Associateship award. The System for Atmospheric Modeling (SAM) was graciously provided by Marat Khairoutdinov (Stony Brook University). No data were used in this work. The large eddy simulation output is available at https://www.esrl.noaa.gov/csd/groups/csd2/clouds/.

References

Bender, F. A.-M., R. J. Charlson, A. M. L. Ekman, and V. Leahy (2011), Quantification of monthly mean regional-scale albedo of marine stratiform clouds in satellite observations and GCMs, *J. Appl. Meteorol. Climatol.*, *50*, 2139–2148.

Benner, C. T., and J. A. Curry (1998), Characteristics of small tropical cumulus clouds and their impact on the environment, *J. Geophys. Res.*, *103*, 28,753–28,767.

Boers, R., and R. M. Mitchell (1994), Absorption feedback in stratocumulus clouds Influence on cloud top albedo, *Tellus A*, *46*, 229–241, doi:10.1034/j.1600-0870.1994.00001.X.

Bohren, C. F. (1980), Multiple scattering of light and some of its observable consequence, *Am. J. Phys.*, *55*, 524–533.

Charlock, T. P., and V. Ramanathan (1985), The albedo field and cloud radiative forcing produced by a general-circulation model with internally generated cloud optics, *J. Atmos. Sci.*, *42*(13), 1408–1429.

Considine, G., J. A. Curry, and B. Wielicki (1997), Modeling cloud fraction and horizontal variability in marine boundary layer clouds, *J. Geophys. Res.*, *102*(D12), 13,517–13,525.

Dawe, J. T., and P. H. Austin (2012), Statistical analysis of an LES shallow cumulus cloud ensemble using a cloud tracking algorithm, *Atmos. Chem. Phys.*, *12*, 1101–1119, doi:10.5194/acp-12-1101-2012.

Donohoe, A., and D. S. Battisti (2011), Atmospheric and surface contributions to planetary albedo, *J. Clim.*, *24*, 4402–4418, doi:10.1175/2011JCLI3946.1.

Engström, A., F. A.-M. Bender, R. J. Charlson, and R. Wood (2015), The nonlinear relationship between albedo and cloud fraction on near-global, monthly mean scale in observations and in the CMIP5 model ensemble, *Geophys. Res. Lett.*, *42*, 9571–9578, doi:10.1002/2015GL066275.

Feingold, G., A. McComiskey, D. Rosenfeld, and A. Sorooshian (2013), On the relationship between cloud contact time and precipitation susceptibility to aerosol, *J. Geophys. Res. Atmos.*, *118*, 10,544–10,554, doi:10.1002/jgrd.50819.

Feingold, G., I. Koren, T. Yamaguchi, and J. Kazil (2015), On the reversibility of transitions between closed and open cellular convection, *Atmos. Chem. Phys.*, *15*, 7351–7367, doi:10.5194/acp-15-7351-2015.

Feingold, G., A. McComiskey, T. Yamaguchi, J. Johnson, K. Carslaw, and K. S. Schmidt (2016), New approaches to quantifying aerosol influence on the cloud radiative effect, *Proc. Natl. Acad. Sci. U.S.A.*, *113*, 5812–5819. [Available at http://www.pnas.org/cgi/doi/10.1073/pnas.1514035112].

Ghan, S., et al. (2016), Challenges in constraining anthropogenic aerosol effects on cloud radiative forcing using present-day spatiotemporal variability, *Proc. Natl. Acad. Sci. U.S.A.*, *113*, 5804–5811.

Harte, J. (2002), Towards a synthesis of the Newtonian and Darwinian worldviews, *Phys. Today*, *55*, 29–34.

Heus, T., and A. Seifert (2013), Automated tracking of shallow cumulus clouds in large domain, long duration large eddy simulations, *Geosci. Model Dev.*, *6*, 1261–1273, doi:10.5194/gmd-6-1261-2013.

Heus, T., H. J. J. Jonker, H. E. A. Van den Akker, E. J. Griffith, M. Koutek, and F. H. Post (2009), A statistical approach to the life-cycle analysis of cumulus clouds selected in a virtual reality environment, *J. Geophys. Res.*, *114*, D06208, doi:10.1029/2008JD010917.

Jiang, H., G. Feingold, and I. Koren (2009), Effect of aerosol on trade cumulus cloud morphology, *J. Geophys. Res.*, *114*, D11209, doi:10.1029/2009JD011750.

Khairoutdinov, M. F., and D. A. Randall (2003), Cloud resolving modeling of the ARM summer 1997 IOP: Model formulation, results, uncertainties, and sensitivities, *J. Atmos. Sci.*, *60*, 607–625.

Koren, I., L. Oreopoulos, G. Feingold, L. A. Remer, and O. Altaratz (2008), How small is a small cloud, *Atmos. Chem. Phys.*, *8*, 3855–3864.

Lee, D.-K., S.-I. Park, J. K. Lee, and N.-M. Hwang (2007), A theoretical model for digestive ripening, *Acta Mater.*, *55*, 5281–5288, doi:10.1016/j.actamat.2007.05.048.

Lenschow, D. H., and P. L. Stephens (1980), The role of thermals in the convective boundary layer, *Boundary Layer Meteorol.*, *19*, 509–532.

Lopez, R. E. (1977), The lognormal distribution and cumulus cloud populations, *Mon. Weather Rev.*, *105*, 865–872.

Lu, M.-L., A. Sorooshian, H. H. Jonsson, G. Feingold, R. C. Flagan, and J. H. Seinfeld (2009), Marine stratocumulus aerosol-cloud relationships in the MASE-II experiment: Precipitation susceptibility in eastern Pacific marine stratocumulus, *J. Geophys. Res.*, *114*, D24203, doi:10.1029/2009JD012774.

Malkus, J. S. (1953), Some results of trade cumulus cloud investigation, *J. Meteorol.*, *11*, 220–237.

Malkus, J. S., and R. H. Simpson (1964), Modification experiments on tropical cumulus clouds, *Science*, *145*, 541–548.

Neggers, R. A. J., H. J. J. Jonker, and A. P. Siebesma (2003), Size statistics of cumulus cloud populations in large-eddy simulations, *J. Atmos. Sci.*, *60*, 1060–1074.

Nober, F. J., and H. F. Graf (2005), A new convective cloud field model based on principles of self-organisation, *Atmos. Chem. Phys.*, *5*, 2749–2759, doi:10.5194/acp-5-2749-2005.

Rauber, R. M., et al. (2007), Rain in shallow cumulus over the ocean: The RICO campaign, *Bull. Am. Meteorol. Soc.*, *88*, 1912–1928.

Romps, D. M., and Z. Kuang (2010), Nature versus nurture in shallow convection, *J. Atmos. Sci.*, *67*, 1655–1666.

Schneider, S. H., and R. E. Dickinson (1976), Parameterization of fractional cloud amounts in climatic models: The importance of modeling multiple reflections, *J. Appl. Meteorol.*, *15*, 1050–1056.

Sharon, T. M., B. A. Albrecht, H. Jonsson, P. Minnis, M. M. Khaiyer, T. M. VanReken, J. Seinfeld, and R. Flagan (2006), Aerosol and cloud microphysical characteristics of rifts and gradients in maritime stratocumulus clouds, *J. Atmos. Sci.*, *63*, 983–997.

Siebesma, A. P., et al. (2003), A large eddy simulation intercomparison study of shallow cumulus convection, *J. Atmos. Sci.*, *60*, 1201–1219.

Stephens, G. L. (1978), Radiation profiles in extended water clouds: II. Parameterization schemes, *J. Atmos. Sci.*, *35*, 2123–2132.

Stevens, B. (2005), Atmospheric moist convection, *Annu. Rev. Earth Planet. Sci.*, *32*, 605–643.

Wang, H., and G. Feingold (2009), Modeling mesoscale cellular structures and drizzle in marine stratocumulus. Part I: Impact of drizzle on the formation and evolution of open cells, *J. Atmos. Sci.*, *66*, 3237–3255.

Witte, M. K., P. Y. Chuang, and G. Feingold (2014), On clocks and clouds, *Atmos. Chem. Phys.*, *14*, 6729–6738, doi:10.5194/acp-14-6729-2014.

Wood, R. (2012), Stratocumulus clouds, *Mon. Weather Rev.*, *140*, 2373–2423.

Wood, R., and P. R. Field (2011), The distribution of cloud horizontal sizes, *J. Clim.*, *24*, 4800–4816.

Wood, R., and D. L. Hartmann (2006), Spatial variability of liquid water path in marine boundary layer clouds: The importance of mesoscale cellular convection, *J. Clim.*, *19*, 1748–1764.

Wood, R., and J. P. Taylor (2001), Liquid water path variability in unbroken marine stratocumulus, *Q. J. R. Meteorol. Soc.*, *127*, 2635–2662.

Xue, H., and G. Feingold (2006), Large eddy simulations of trade wind cumuli: Investigation of aerosol indirect effects, *J. Atmos. Sci.*, *63*, 1605–1622.

Xue, H., G. Feingold, and B. Stevens (2008), Aerosol effects on clouds, precipitation, and the organization of shallow cumulus convection, *J. Atmos. Sci.*, *65*, 392–406.

Yamaguchi, Y., and G. Feingold (2015), On the relationship between open cellular convective cloud patterns and the spatial distribution of precipitation, *Atmos. Chem. Phys.*, *15*, 1237–1251, doi:10.5194/acp-15-1237-2015.

Zhao, G., and L. Di Girolamo (2007), Statistics on the macrophysical properties of trade wind cumuli over the tropical western Atlantic, *J. Geophys. Res.*, *112*, D10204, doi:10.1029/2006JD007371.